

Spider-Web-Inspired PM_{0.3} Filters Based on Self-Sustained Electrostatic Nanostructured Networks

Shichao Zhang, Hui Liu, Ning Tang, Sheng Zhou, Jianyong Yu, and Bin Ding*

Particulate matter (PM) pollution has become a serious public health issue, especially with outbreaks of emerging infectious diseases. However, most present filters are bulky, opaque, and show low-efficiency PM_{0.3}/pathogen interception and inevitable trade-off between PM removal and air permeability. Here, a unique electrospaying–netting technique is used to create spider-web-inspired network generator (SWING) air filters. Manipulation of the dynamic of the Taylor cone and phase separation of its ejected droplets enable the generation of 2D self-charging nanostructured networks on a large scale. The resultant SWING filters show exceptional long-range electrostatic property driven by aeolian vibration, enabling self-sustained PM adhesion. Combined with their Steiner-tree-structured pores (size 200–300 nm) consisting of nanowires (diameter 12 nm), the SWING filters exhibit high efficiency (>99.995% PM_{0.3} removal), low air resistance (<0.09% atmosphere pressure), high transparency (>82%), and remarkable bioprotective activity for biohazard pathogens. This work may shed light on designing new fibrous materials for environmental and energy applications.

small airways, and carry various bacteria/viruses.^[4–6] Most emerging infectious diseases (EIDs) are transmitted by the airborne PM route, such as 2019 novel coronavirus (COVID-19) that has spread rapidly worldwide.^[7–9] Measures taken by the public to protect from PM pollution and EID transmission, are mostly focused on fibrous filters, for example, face mask, air purifier, etc.^[6,10] Unfortunately, the commonly used microfiber air filters (melt-blown and glass fibers) usually suffer from poor PM_{2.5} removal efficacy (much worse for MPPS PM_{0.3}), high energy consumption due to their micrometer-sized fiber diameters (5–50 μm) and low porosity (<60%). Compared with the microfiber counterparts, nanofiber filters have a unique advantage due to their dramatically reduced diameters (usually <1 μm), which give them reduced pore sizes and improved porosities to enhance

Atmospheric particulate matter (PM) pollution constitutes the forefront of global safety concerns, which leads to serious environmental issues, and poses huge burden to the global economy and public health.^[1–3] PM, as a complex mixture, is typically categorized as PM₁, PM_{2.5}, and PM₁₀, which refer to particle sizes below 1, 2.5, and 10 μm, respectively. PM_{0.3}, PMs with the most penetrating particle size (MPPS, ≈300 nm), is especially notorious because it can travel long distances, penetrate


both removal capacity and air permeability.

To construct the cutting-edge nanofiber filters, two types of building blocks—electrospun nanofibers and carbon nanotubes—are used in common. Despite the improved air permeability, the electrospun nanofiber filters showed limited removal efficiency, especially for MPPS PM_{0.3}, due to pseudo-nanoscale diameters (0.2–2 μm), and random stacking structures with large pore sizes (usually >3 μm) caused by uncontrolled spinning–deposition manner.^[11–13] High PM capture efficiency has been achieved using carbon nanotubes (5–50 nm in diameter) at the expense of high air resistance, since they inevitably stack compactly due to poor structural continuity and dispersity.^[14–16] Nature provides a bio-inspiration associated with filter construction: creating fibrous network structures can dramatically improve material utilization and the resultant properties.^[17–19] The natural dusty spider webs are vivid case of nature power. To mimic the spider web structures at nanoscale, previously, pieces of 2D web-like structures with fiber diameter (<50 nm), were found in our group.^[20,21] However, these structures were only an unpredictable, occasionally formed (<2% content) accessory product accompanying defective micro/nanofibers. And they were partly nonporous, showed compact stacking structures, leading to fatal obstacle for their utilization as air filters. Inspired by the dusty spider dragline silk, assembling an ordered nanostructured fibrous network with stickiness could remove PMs with high efficiency and low air resistance; however, design of such filters is extremely challenging.

Dr. S. C. Zhang, Dr. H. Liu, Dr. N. Tang, Prof. J. Y. Yu, Prof. B. Ding
State Key Laboratory for Modification of Chemical Fibers
and Polymer Materials
College of Textiles
Donghua University
Shanghai 201620, China
E-mail: binding@dhu.edu.cn

Dr. S. C. Zhang, Dr. H. Liu, Prof. J. Y. Yu, Prof. B. Ding
Innovation Center for Textile Science and Technology
Donghua University
Shanghai 200051, China

Dr. S. C. Zhang, Dr. S. Zhou
Department of Orthopedics
School of Medicine
West Virginia University
Morgantown, WV 26506, USA

 The ORCID identification number(s) for the author(s) of this article can be found under <https://doi.org/10.1002/adma.202002361>.

DOI: 10.1002/adma.202002361

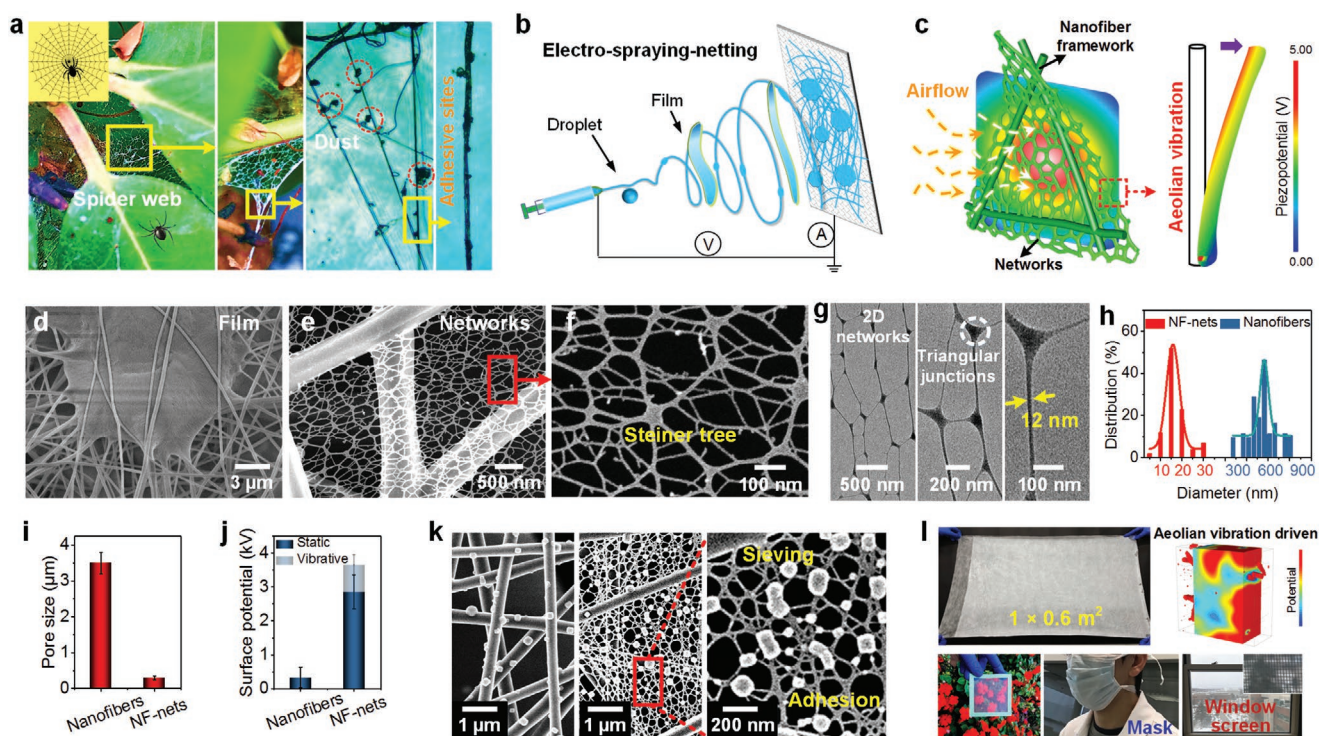


Figure 1. a) A set of optical photographs showing the natural spider web adhering numerous tiny dust particles. b) Schematic showing the electro-spraying–netting technique. c) Schematic illustration of (left) the self-sustained electrostatic SWING filters due to airflow stimuli and (right) potential distribution for a single nanowire in 2D networks due to aeolian vibration. d,e) SEM images of nanofiber/film (d) and NF-net (e) membranes. f) High-magnification SEM image of 2D NF-nets. g) TEM images of the NF-nets and their nanostructures. h–j) Comparisons of fiber diameters (h), pore size (i), and surface potential (j) of PVDF nanofiber and NF-net filters. k) SEM images of PVDF nanofiber and NF-net filters after PM filtration (airflow velocity of 20 cm s^{-1}). l) The photograph of the large-sized PVDF-NF-net membrane and its fabricated samples (medical masks and transparent window screens) for various applications.

Inspired by the adhesive draglines and ordered networks in natural spider webs, herein, we reported a facile methodology to create spider-web-inspired network generator (SWING) air filters, based on unique electro-spraying–netting technique. The advantage of the design is that the droplet ejection/phase separation and crystal phase transition are both manipulated to develop 2D continuously welded nanostructured networks (nanowire diameter of 12 nm) with self-sustained long-range electrostatic adhesion. The resultant SWING filters showed integrated properties of small pore size (200–300 nm) and innovative self-charging capacity (3.7 kV surface potential), enabling the synergistic effect of physical sieving and electrostatic adhesion for PM removal. As expected, high efficiency (>99.995%), low pressure drop (<88.5 Pa), high transparency (>82%), robust bioprotective activity, energy-saving, and long-term stability for MPPS $\text{PM}_{0.3}$ /pathogen removal were achieved, all originating from the nanosize effect of 2D self-sustained electrostatic networks.

Natural spider web displays ordered network structures consisting of adhesive dragline silks that help catch its preys and remain stable against high-speed wind (Figure 1a). Inspired by the dusty spider web, biomimetic 2D nanostructured fibrous networks (NF-nets) were developed into high-performance air filters, using our innovative electro-spraying–netting technique (Figure 1b). We chose poly(vinylidene fluoride) (PVDF) as raw material to construct NF-net filters, in considering its

outstanding characteristics, such as robust mechanical property, strong piezoelectric property, and high thermal/chemical stability. The creation of NF-nets was due to a droplet spray–deformation–assembly process that driven by Taylor cone instability and incomplete phase separation. The resultant NF-nets show two unique characteristics (Figure 1c): i) the 2D networks supported by scaffold nanofibers endow filters with maximal PM removal efficacy and mechanical strength yet retaining high air/light penetrability (Figure 1c, left); ii) the self-charging piezoelectric β -phase PVDF nanowires in NF-nets based on aeolian vibration allow the synergistic effect of sieving and adhesion for PM removal (Figure 1c, right). Our utilized electro-spraying–netting is a unique but universal methodology compared to other electrohydrodynamic techniques. During electro-spraying–netting process, the charged droplets ejected from a Taylor cone, and then deformed and evolved into pieces of film/networks (Figure 1d; Figure S1, Supporting Information); in contrast, the jets ejected and formed micro/nanofibers during electrospinning (Figure S2a, Supporting Information). Unlike conventional electro-spraying that usually generated microparticles,^[22] tailoring of the precursor solution allowed the droplets to synchronously deform and phase separate to form a 2D network architecture (Figure 1e,f).

Scanning electron microscopy (SEM) imaging (Figure 1e,f) indicates that the PVDF NF-nets consist of 1D nanowires with diameters of 5–30 nm and show 2D topological Steiner tree

structures. A closer transmission electron microscopy (TEM) look (Figure 1g) demonstrates that the nanowires are highly interconnected with each other through triangular junctions, exhibiting unique 2D lateral infinity. Strikingly, the nanowire diameter in NF-nets is true nanoscale (average 12 nm). Such diameter is at least one order of magnitude less than those of conventional nanofibers (>300 nm; Figure 1h; Figure S2, Supporting Information), providing the nanoeffect potential. Due to 2D network topography, the NF-nets exhibited extremely small pore sizes of 200–300 nm compared to >3 μm of conventional electrospun nanofibers (Figure 1i). Besides, during electrospaying–netting, abundant dipoles in PVDF molecules were aligned due to the in situ charging effect and strong mechanical stretching of nanowires in NF-nets,^[23,24] suggesting self-sustained and high surface potential (2.8 kV, even 3.7 kV after aeolian vibration activation; Figure 1j). In dramatic contrast to weak short-range intermolecular forces in polar polymeric nanofibers previously used for air filtration,^[13,25] the self-charging piezoelectric PVDF NF-nets showed robust long-range electrostatic forces. Thus, both their structural sieving and electrostatic adhesion capabilities were enhanced >10 times, which was confirmed by SEM observation after PM removal (Figure 1k). And, the NF-nets showed desirable structural stability without any damage under high airflow velocity (20 cm s⁻¹). No such self-sustained electrostatic filters have ever been reported before. Due to the simplicity of electrospaying–netting technique, scaling up the assembly of NF-nets was feasible; a PVDF NF-net membrane with size of 1 × 0.6 m² was prepared (Figure 1l). Besides high-performance PM removal capacity, the resultant spider-web-inspired network generator (SWING)-based filters were highly transparent, suggesting widespread applications in areas of individual protection, indoor purification, etc. Now some industrial samples (such as face mask and window screen), using NF-nets as core components, were fabricated (Figure 1l, bottom).

Our innovative electrospaying–netting route includes two processes of droplet ejection and deformation/phase separation. To reveal the ejection of the droplets from Taylor cone, we developed a numerical model based on the force competition between Coulombic repulsion and hydrostatic pressure (Table S1 and Section S3, Supporting Information). This ejection of Taylor cone involves two typical modes (i.e., jet and droplet ejections). Here, tailoring of PVDF concentrations was utilized to control the charge densities of the liquids (Section S2, Supporting Information), then to regulate the dynamics of Taylor cone. A numerical diagram for droplet/jet ejection was established, as shown in Figure 2a and Figure S3 (Supporting Information). With increasing PVDF concentrations (12–21 wt%), both the theoretically required jet threshold J_c ($\sqrt{64\epsilon\gamma/\rho^2 D^3}$) and droplet threshold D_c ($\sqrt{288\epsilon\gamma/\rho^2 D^3}$) decreased (J_c , from 0.45 to 0.1 c kg⁻¹; D_c , from 0.94 to 0.2 c kg⁻¹) significantly (where ϵ is the ambient permittivity, γ is the surface tension of fluid, ρ is the fluid density, and D is the diameter of Taylor cone apex). This change meant the ejection of charged droplets was initiated when the actual charge density raised higher than the required droplet threshold (18 and 21 wt% PVDF solutions). SEM observation was also conducted to verify our model predictions (Figure 2b). In contrast to the microparticles and beaded nanofibers (12-0 and 15-0 systems), abundant solid films

formed from 18-0 and 21-0 PVDF solutions. We think these films were derived from the ejected droplets, which generated when their charge densities were larger than the corresponding droplet thresholds.

To mimic the functional spider web, these resultant architectures should be processed into porous network structures, rather than nonporous solid films. This requirement was satisfied by control of phase separation of the deformed droplets. As illustrated in Figure 2c, along with solvent evaporation, the addition of dodecyltrimethylammonium bromide (DTAB) in PVDF solutions caused incomplete phase separation, generating randomly distributed polymer-rich regions and continuous solvent-rich regions. The bottom insets in Figure 2c depict the evolution of optical morphology of PVDF/DTAB solutions. Innovatively, this strategy supported the transition from solid films to porous networks. Evidence of the formation process of 2D networks driven by phase separation also arose from SEM observations (Figure 2d) of the architectures obtained at different tip–collector distances (TCDs, 5, 15, and 25 cm). The phase separation of the droplets after adequate flight process enabled the generation of 2D porous NF-nets. In addition, a facile method, by monitoring the solution transmittance during solvent evaporation, to capture their dynamics of phase separation, was utilized (Section S2, Supporting Information). Figure 2e and Figure S4 (Supporting Information) present the relative transmittance (RT) and its deviation curves, that deduced from gray level analysis of the microscopic images of different solutions over time. Pure PVDF solutions exhibited the slowest growth rate in RT deviation, indicating a homogeneous solution phase (Figure S5, Supporting Information). While, solvent evaporation shifted the PVDF/DTAB solutions, such as 18-2 and 18-4 systems, into spinodal decomposition state, leading to an obvious heterogeneity (i.e., larger slope of RT deviation curves). As expected, SEM results of the architectures were consistent with the phase transition analysis of their precursor solutions. As shown in Figure 2f, deficient (18-0.5 and 18-1 systems) and excessive (18-4 system) phase separations resulted in partially nonporous defects and broken fibrils, respectively. And the coverage rates of the network structures in these membranes were limited (≈45%, ≈75%, and ≈88%, respectively). In contrast, the fully covered (≈100%) networks with ideal/weight Steiner tree structures were easily obtained (18-2 system); and they were continuously welded, interlinked with each other, and tightly bonded with scaffold nanofibers.

The nanowire diameters (≈12 nm) and lateral infinity of 2D NF-nets, allowed the resultant membranes to exhibit greatly improved Brunauer–Emmett–Teller (BET)-specific surface area of 45 m² g⁻¹ and porosity of 99.5% compared to <15 m² g⁻¹ and <70% of PVDF nanofibers (Figure 3a). Manipulation of NF-net contents by control of DTAB concentrations enabled an obvious decrease in the pore sizes of the membranes (from 4.5 μm to 200–300 nm), as shown in Figure 3b and Figure S6 (Supporting Information). These integrated pores were much stable and at least one order of magnitude smaller than those of conventional stacking nanofibers, and thus fundamentally enhanced the sieving properties of the filters. Strikingly, such pore size range meant the NF-nets had intrinsic advantages for capturing MPPS PMs with ≈300 nm in size. The presence of DTAB that mostly located on the fiber surfaces probably allowed the NF-nets to provide ionic sites for air filtration due to their

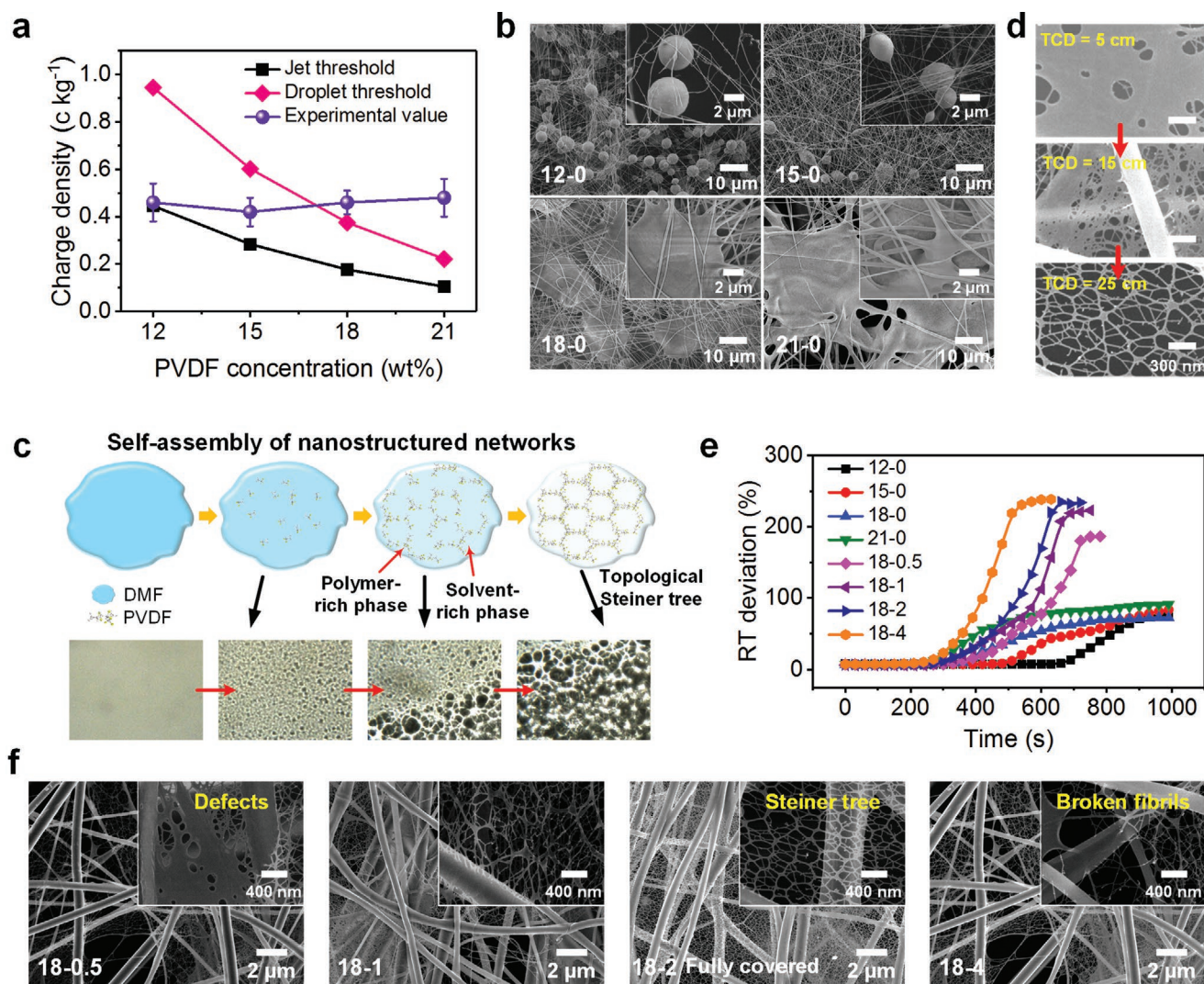


Figure 2. a) Charge densities of the fluids and b) SEM images of the nanomaterials obtained from solutions with different PVDF concentrations. c) Self-assembly of the NF-nets through deformation and phase separation of the charged droplets. d) Evolution of phase separation of the liquid film derived from the droplet during electrospinning–netting. Top to bottom: SEM images of the deposited architectures obtained at TCDs of 5, 15, and 25 cm. e) Relative transmittance (RT) deviation as a function of time for various PVDF/DTAB solutions. f) SEM images of the PVDF NF-net membranes obtained with various DTAB concentrations: X–Y in (b), (e), and (f), where X and Y are PVDF and DTAB concentrations (wt%), respectively.

exposing hydrophilic groups (Figure S7, Supporting Information).^[25] Both Fourier transform infrared (FTIR) spectra and X-ray diffraction (XRD) patterns (Figure 3c,d) indicate that our electrospinning–netting process caused an obvious crystal phase transition from α -phase to β -phase for PVDF NF-nets. As presented in Figure 3e, the generation of 2D NF-nets led to significantly improved content of β -phase (85.3%, determined by FTIR analysis) in contrast to the control nanofibers (48.3%). We attributed this result to the synergetic effect of the nanoscale diameter, uniaxially mechanical stretching, rapid solidification (Figure S1, Supporting Information), and ion-dipole interaction.^[23,26] Thus, their surface potentials increased from 0.33 to 2.85 kV, almost ten times improvement, due to the increased content of self-polarized NF-nets. The combination of large BET surface area and remarkable electrostatic property, which were synergistic, provided the ability to tightly capture PMs on PVDF nanowires without falling off, even under

high-velocity airflow. Many new energy applications highly demand flexible and efficient electromechanical conversion materials.^[27,28] Piezoelectric PVDF, especially their β -phase, was attractive and widely used;^[29] however, most PVDF nanomaterials showed piezoelectric coefficient d_{33} of -20 to -30 pm V⁻¹. In contrast, the PVDF NF-nets exhibited a d_{33} of -45 pm V⁻¹ and a dielectric constant of 11.1 (Figure 3f), indicating their promising applications for electromechanical sensors, transducers, and mechanical energy harvesters.

Despite exceptional tensile strength of some single nanofibers, most present nanofiber materials, in particular, nonwoven membranes, are devoid of enough mechanical strength, usually <10 MPa.^[30] The tensile stress–strain curves (Figure 3g) show a strong positive correlation between the tensile strength and NF-net content, implying an innovative strengthen strategy. Compared to the tensile strength of 5 MPa with elongation at break of 45% of PVDF nanofibers (Figure S8,

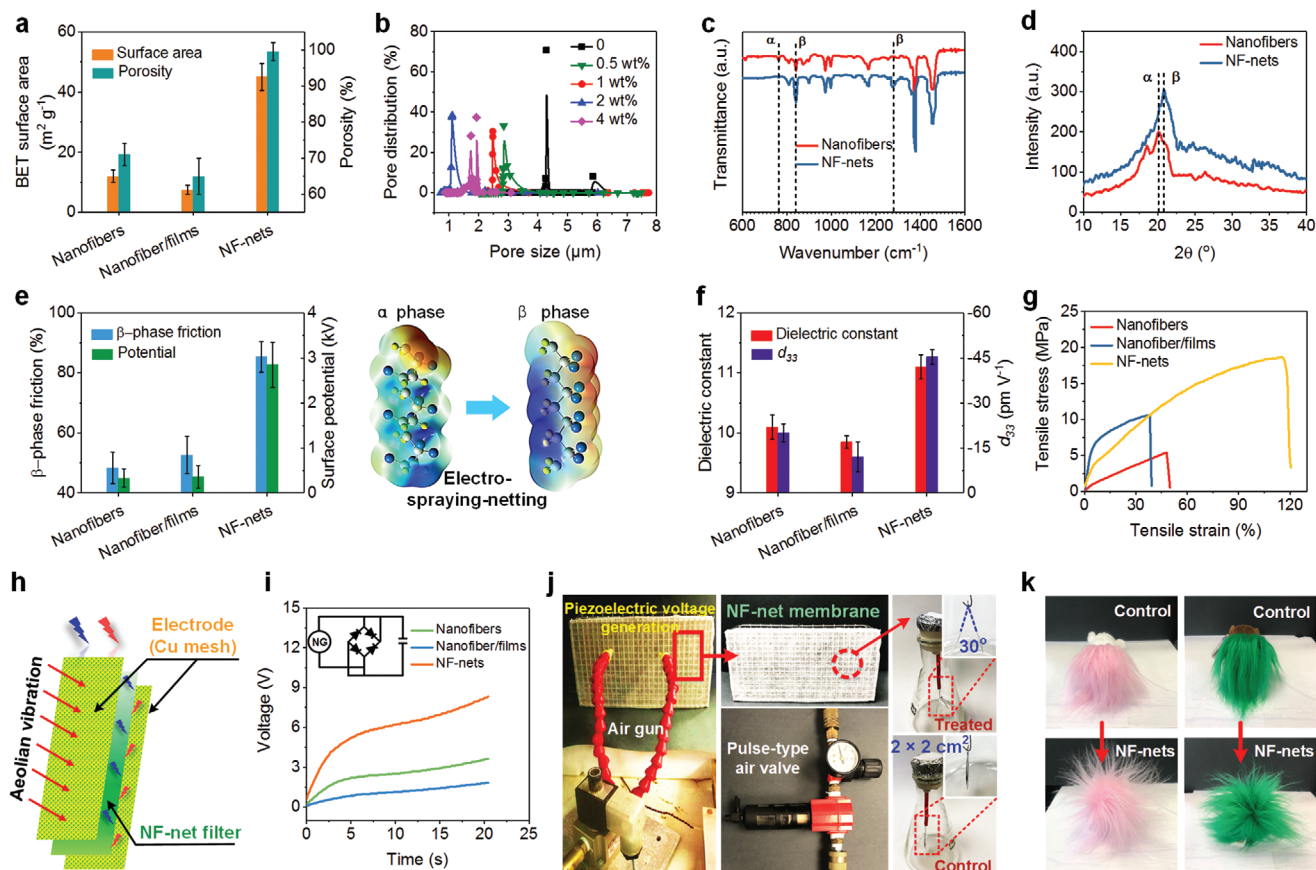


Figure 3. a,e–g,i) Comparison of: a) BET surface areas and porosities, e) β -phase frictions, f) dielectric constants and d_{33} values, g) tensile stresses, and i) piezoelectric charging performances between PVDF nanofiber, nanofiber/film, and NF-net membranes. i) Inset: A schematic of a circuit diagram for capacitor charging of the nanogenerator. b) Pore size distribution of the PVDF NF-net membranes obtained from solutions with various DTAB concentrations. c) FTIR spectra and d) XRD patterns of PVDF nanofiber and NF-net membranes. h) Schematic diagram of the self-charging nanogenerator based on PVDF NF-nets. j) A set of photographs showing the piezoelectric voltage generation of window screens using PVDF NF-net filters due to pulse-type airflow. The electroscopes confirm an obvious charging process of SWING filters due to wind pressure. k) Snapshot images of fluffy toys sitting on the PVDF control nanofiber and SWING filter membranes treated by pulse-type airflow (20 min).

Supporting Information), the NF-net membranes achieved 19.3 MPa strength and 120% break elongation. This change was due to their integrated features of nanoscale diameters, interlinked networks, and a net-bonding effect, which brought rapid stress dissipation paths.^[31,32] To demonstrate the self-sustained electrostatic property of our SWING filters, a simple nanogenerator consist of PVDF NF-net filter and Cu meshes was created (Figure 3h). This NF-net based nanogenerator, as a wind energy harvester, was driven by aeolian vibration, and enabled a high output voltage of 8.3 V under an exerted wind pressure of 150 Pa due to its increased β -phase content (airflow velocity of 5 m s⁻¹; Figure 3i). And the process to charge a 1 μ F capacitor to over 6 V was quite fast, only 20 s. In contrast, PVDF nanofiber based nanogenerator can only achieve 1.5 V under the same wind pressure. An increase in wind velocity from 0.2 to 5 to 10 m s⁻¹ resulted in an increase of the output voltage from 0.075 to 8.3 to 20.5 V. This result indicated that such SWING filters were an autofretage design, which meant high airflow velocity enabled their enhanced electrostatic adhesion for PM removal. For better illustration, a set of optical images showing the piezoelectric voltage generation of SWING window screens

due to pulse-type airflow (to mimic natural breeze) were presented in Figure 3j. After 20 min, the output voltage of NF-net membranes (2 \times 2 cm²) enabled two foils (\approx 0.05 g) in a simple electroscopes to be mutually exclusive (opening angle of 30°). In contrast, the foil opening angle using control nanofiber membranes was negligible (<3°). Visually, the fluffy toys instantaneously exhibited a status of “wild-curl up” when put them on NF-net membranes charged by aeolian vibration activation (Figure 3k), revealing the strong long-range electrostatic force.

Intelligibly, the easier leakage typically happened to the smaller PMs for filters, yet, such PMs usually caused higher risks.^[33–35] Besides PM_{2.5}, we challenged the filters with PM₁ and MPPS PM_{0.3} (PM concentration of 300 000–500 000). As illustrated in Figure 4a and Figure S7 (Supporting Information), in contrast to the nanofiber and nanofiber/film filters, our SWING filters exhibited higher removal efficiency for all kinds of PMs. They achieved 65.224%, 98.332%, and 99.003% for capturing PM_{0.3}, PM₁, and PM_{2.5}, respectively, indicating almost three times higher compared to their counterparts. Meanwhile, the SWING filters maintained low air resistance (5.5 Pa) and high quality factor (up to 0.8; Figure S9 and Table S2, Supporting

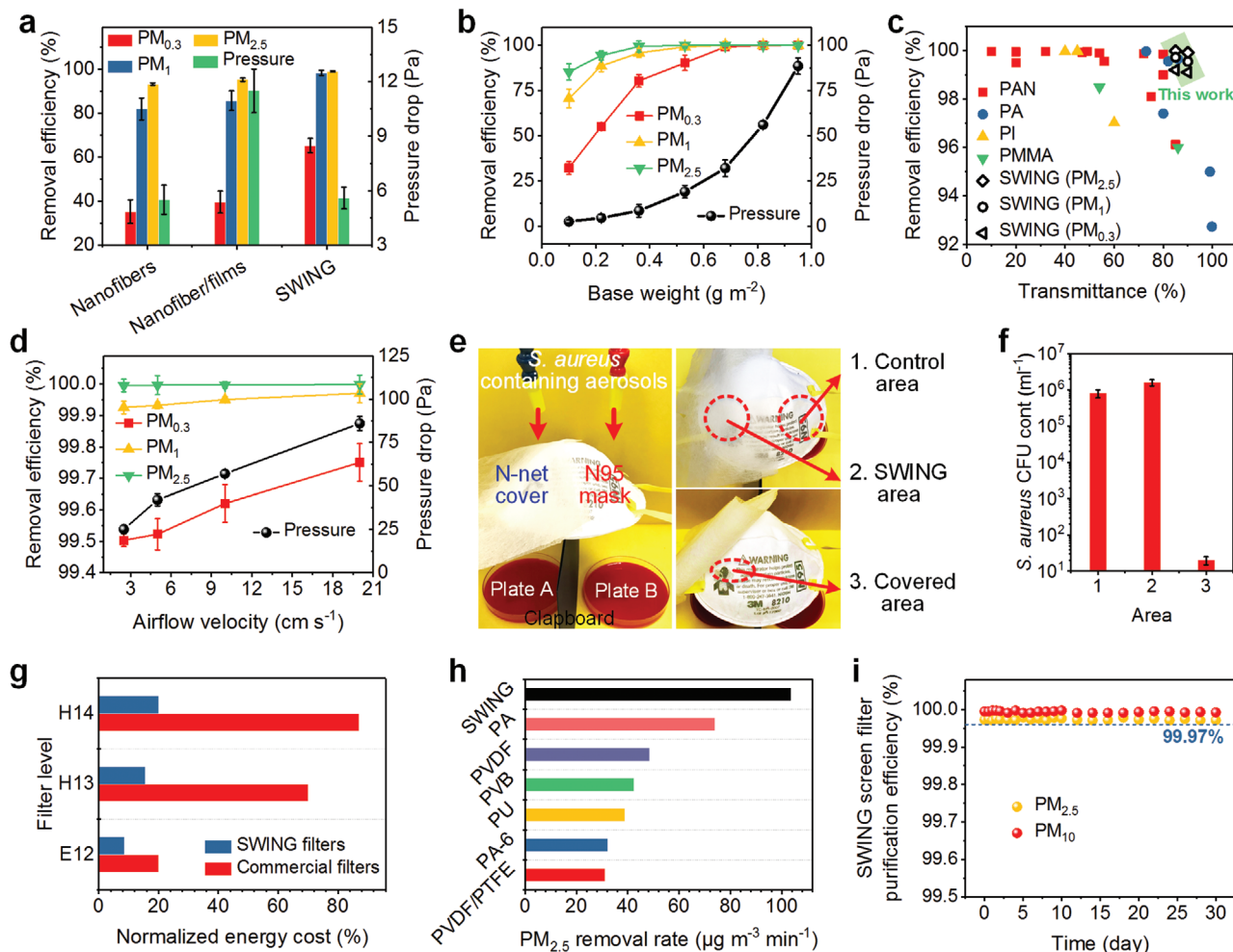


Figure 4. a) NaCl $PM_{0.3}$, PM_{1} , and $PM_{2.5}$ removal efficiencies and pressure drops of PVDF nanofiber, nanofiber/film, and SWING air filters. Airflow velocity used in (a), 5.33 cm s^{-1} . Filter base weight used in (a), $\approx 0.3 \text{ g m}^{-2}$. b,d) PM removal efficiencies and pressure drops of the SWING filters with various base weights (b) and under various airflow velocities (d). Airflow velocity used in (b), 5.33 cm s^{-1} . Filter base weight used in (d), $\approx 0.75 \text{ g m}^{-2}$. c) The removal efficiencies of selected nanofiber materials at different transmittance values. e) Interception test for removing *S. aureus*-containing PMs by the SWING filter and N95 mask. f) The CFU count of *S. aureus* of three selected areas on the filter or mask indicated in (e). g) Comparison of energy cost between commercial filters and the SWING filters. h) Comparison of $PM_{2.5}$ removal rates between PVDF SWING filters and other filtration materials. i) Long-term field test (Shanghai) performance of SWING window screens for $PM_{2.5}$ and PM_{10} removal.

Information). Counterintuitively, PM removal efficiency and air permeability of our SWING filters are both high, in contrast to the trade-off behavior of traditional air filters, where higher removal efficiency invariably leads to higher air resistance.^[36] We believed such performances were due to 2D adhesive NF-nets, a structure that synchronously enhanced PM capture by small pore sizes and electrostatic adhesion, and reduced drag force of airflow based on “slip-effect” originating from nanowires.^[16] Their airflow “slip-effect” was enhanced >10 times with Knudsen number of 8.8 (Table S3, Supporting Information), compared to conventional nanofibers. Facile increasing of base weights allowed the SWING filters to achieve significantly improved removal levels (Figure 4b). Our filters with light-weight of 0.95 g m^{-2} can removal MPPS $PM_{0.3}$ with 99.995% efficiency and $PM_{2.5}$ with 100% efficiency; such superior performance has rarely been achieved previously. Besides the rigid NaCl PMs, this performance can be maintained for capturing

soft oil-based di(2-ethylhexyl) sebacate particles (Figure S10, Supporting Information). Even with increasing NaCl PM concentration from 0.5 to 20 million, the SWING filters exhibited only a slight decrease in removal efficiency, for example, from 99.995% to 99.991% for $PM_{0.3}$ removal (Figure S11, Supporting Information). More strikingly, their air resistances were <88.5 Pa, only <0.09% of atmosphere pressure, which was negligible.

Besides filtration capacity, the other important property of high-performance air filters, light transmittance, was assessed (Figure 4c). Most existing transparent filters were used to filtrate relatively large PMs ($PM_{2.5}$ and PM_{10}), and exhibited a limited transmittance (<80%) and relatively high air resistance (>200 Pa).^[12,13,25,37] In contrast, by virtue of their unique 2D networks, light weight, and thin thickness, the SWING filters showed much better transmittance and stronger removal capacity for the smaller and more penetrating PMs ($PM_{0.3}$ and PM_{1}).

They achieved >99.98% PM_{2.5}, >99.72% PM₁, and >99.21% PM_{0.3} removals, while maintaining 90% transmittance, indicating the promising potential for electrical devices, bioengineering, optical imaging, etc. Unlike conventional fibrous filters that usually suffered from performance deterioration under high wind speed, the SWING filters exhibited improving removal efficiencies for all PMs with increasing airflow velocities (Figure 4d). Under a high velocity of 20 cm s⁻¹, the filters showed stable and higher capture efficiencies for PM_{0.3} (>99.75%), PM₁ (>99.97%), and PM_{2.5} (>99.99%). In contrast, their removal efficiencies were 99.5%, 99.92%, and 99.98% for PM_{0.3}, PM₁, and PM_{2.5} under velocity of 2.5 cm s⁻¹. Such unique performance was ascribed to the self-sustained design of self-charging piezoelectric SWING filters, in which higher wind speeds enabled stronger long-range electrostatic force for PM capture.

The outbreak of the EID of COVID-19 has caused serious global health issues.^[38,39] Airborne PMs, especially MPPS PM_{0.3}, as a major medium carrying bacteria/viruses, can be easily adsorbed by human respiratory and cardiovascular systems, leading to serious EID spread. In considering the remarkable PM_{0.3} removal efficacy based on physical sieving and long-range electrostatic adhesion, the utilization of SWING filters as a core function layer for bioprotection applications, was promising. We challenged the SWING filters with clinical *Staphylococcus aureus*. To mimic the sneeze or cough particles from infectious individuals, 1 × 10⁶ colony forming units (CFU) of *S. aureus*-containing aerosols (0.3–5 μm) were generated and utilized. As illustrated in Figure 4e, the left half part of a 3M 8210 mask was shielded using a SWING filter membrane, the agar plates placed below the mask were used to detect *S. aureus* leakage. The testing process was performed by exposing the mask to a 1 mL min⁻¹ of *S. aureus*-containing PM airflow for 30 min. The *S. aureus* proliferation on plates showed that abundant *S. aureus*-containing PMs penetrated through N95 mask, in contrast, almost no bacterial leakage was found using the SWING filter cover. After filtrating 1 mL min⁻¹ *S. aureus* PMs for 1 min, three areas (1 × 1 cm²) including control area, SWING area, and covered area were harvested and evaluated. As shown in Figure 4f, >2 times *S. aureus*-containing PMs were captured by SWING filters compared to the N95 mask, resulting in that almost no *S. aureus* (<20 CFU ml⁻¹) was detected on the covered area. Moreover, the filtration performance and mechanical property of the SWING filters remained almost unchanged after exposing to ultraviolet (UV; 280–285 nm) for 24 h (Figure S12a,b, Supporting Information), confirming its remarkable long-term stability in real outdoor environment. Strikingly, using a facile UV irradiation, most of the captured *S. aureus* on the filters could be killed due to the high transmittance and surface filtration manner (Figure S12c, Supporting Information). Obviously, our SWING filters, as a shielding layer, significantly improved the filter level, enabled reusability, and prolonged service life, revealing their intriguing applications in bioprotective equipment against EID threats.

Developing new materials to reduce the energy demand for air pollution control is an urgent challenge facing sustainable development.^[40–42] The advantages of the SWING filters were further demonstrated in terms of their energy-saving capacity, purification rate, and long-term stability. Our self-sustained

piezoelectric SWING filters, which were driven by wind energy and showed low air resistance, were a typical energy-saving/harvesting material. Here, we estimated the energy consumption of some representative commercial filters and SWING filters according to the ASHRAE 1996 Handbook: $\varnothing = \nu \Delta Pt / 6356 \omega_1 \omega_2$ is the energy consumption, where ν is the airflow velocity, t is the operation time, ω_1 is the motor efficiency (0.9), and ω_2 is the fan efficiency (0.75). As shown in Figure 4g, substituting market air filters by the SWING filters, the energy costs were reduced by 57.5%, 77.8%, and 78.5% for E12, H13, and H14 level filters, respectively. We also assessed the recyclability of the SWING filters (85% transmittance) for purifying smoke PM_{2.5} and PM₁₀ (size distribution <300 nm → 10 μm). In severely polluted atmosphere (>1000 μg m⁻³ PM_{2.5} and >6000 μg m⁻³ PM₁₀), >80% PM_{2.5} and >90% PM₁₀ were removed using SWING filters within only 3 min. In contrast to the previously reported nanofiber filters (mostly <50 μg m⁻³ min⁻¹), our SWING filters achieved the removal rate of 105 μg m⁻³ min⁻¹ (≈2 times higher) for PM_{2.5} purification (Figure 4h). Surprisingly, such robust removal capacity was quite stable and almost unchanged within 10 cycles (purification from >500 to <35 μg m⁻³ within 5 min), indicating the promising application as window screen. To take into account real weather (like humidity, temperature, and wind), a field test of the SWING filters in Shanghai, China was carried out (Figure 4i). After 30 days, the filters still maintained both >99.97% removal efficiencies for PM_{2.5} and PM₁₀, and their change (from 22 to 23.5 Pa) in air resistances was negligible. In considering that the NF-net membranes could be directly deposited on conventional window screens, we believed our SWING filters provided a simple and cost-effective strategy that could facilitate indoor air purification without sacrificing the fresh air/light penetrability.

In summary, we have demonstrated a concept of self-sustained electrostatic air purifiers (SWING filters) based on spider-web-inspired nanostructured networks. Using unique electro-spraying-netting technique, the ejection and deformation/phase separation of the charged droplets from a Taylor cone were tailored to make them evolve and assemble into 2D NF-nets. Due to the integrated properties of nanowire diameters (≈12 nm), small Steiner-tree-structured pores, exceptional adsorption, and new self-charging design (3.7 kV potential) driven by aeolian vibration, the resultant SWING filters can remove MPPS PM_{0.3} with high efficiency of >99.995%, <0.09% atmosphere pressure, and high transparency of >82%. And they also showed remarkable bioprotective activity for biohazard pathogens, energy-saving capacity, and long-term stability. We envision that our findings provide valuable insights for design and development of high-performance fibrous materials and also open the door for their applications in public health protection.

Experimental Section

Experimental details are available in the Supporting Information.

Supporting Information

Supporting Information is available from the Wiley Online Library or from the author.

Acknowledgements

This work was supported by the National Natural Science Foundation of China (Nos. 51973028 and 51925302), the Fundamental Research Funds for the Central Universities (No. 223201900081), and Donghua University International Postdoctoral Program.

Conflict of Interest

The authors declare no conflict of interest.

Keywords

air filtration, bioprotective equipment, electrospraying–netting, electrostatic, fibrous network, personal protective equipment (PPE)

Received: April 6, 2020

Revised: May 4, 2020

Published online: June 8, 2020

- [1] Q. Zhang, X. Jiang, D. Tong, S. J. Davis, H. Zhao, G. Geng, T. Feng, B. Zheng, Z. Lu, D. G. Streets, *Nature* **2017**, 543, 705.
- [2] A. Nel, *Science* **2005**, 308, 804.
- [3] N. Mahowald, *Science* **2011**, 334, 794.
- [4] R. J. Huang, Y. Zhang, C. Bozzetti, K. F. Ho, J. J. Cao, Y. Han, K. R. Daellenbach, J. G. Slowik, S. M. Platt, F. Canonaco, *Nature* **2014**, 514, 218.
- [5] S. Zhang, H. Liu, N. Tang, N. Ali, J. Yu, B. Ding, *ACS Nano* **2019**, 13, 13501.
- [6] C. Wang, Y. Otani, *Ind. Eng. Chem. Res.* **2013**, 52, 5.
- [7] C. J. E. Metcalf, J. Lessler, *Science* **2017**, 357, 149.
- [8] F. Wu, S. Zhao, B. Yu, Y. M. Chen, W. Wang, Z. G. Song, Y. Hu, Z. W. Tao, J. H. Tian, Y. Y. Pei, *Nature* **2020**, 579, 256.
- [9] K. E. Jones, N. G. Patel, M. A. Levy, A. Storeygard, D. Balk, J. L. Gittleman, P. Daszak, *Nature* **2008**, 451, 990.
- [10] M. Burgard, D. Weiss, K. Kreger, H. Schmalz, S. Agarwal, H. W. Schmidt, A. Greiner, *Adv. Funct. Mater.* **2019**, 29, 1903166.
- [11] K. M. Yun, C. J. Hogan, Y. Matsubayashi, M. Kawabe, F. Iskandar, K. Okuyama, *Chem. Eng. Sci.* **2007**, 62, 4751.
- [12] B. Khalid, X. Bai, H. Wei, Y. Huang, H. Wu, Y. Cui, *Nano Lett.* **2017**, 17, 1140.
- [13] J. Xu, C. Liu, P. C. Hsu, K. Liu, R. Zhang, Y. Liu, Y. Cui, *Nano Lett.* **2016**, 16, 1270.
- [14] G. Viswanathan, D. B. Kane, P. J. Lipowicz, *Adv. Mater.* **2004**, 16, 2045.
- [15] C. Wang, P. Li, Y. Zong, Y. Zhang, S. Li, F. Wei, *Carbon* **2014**, 79, 424.
- [16] P. Li, C. Wang, Y. Zhang, F. Wei, *Small* **2014**, 10, 4543.
- [17] Z. Shao, F. Vollrath, *Nature* **2002**, 418, 741.
- [18] E. Steven, W. R. Saleh, V. Lebedev, S. F. Acquah, V. Laukhin, R. G. Alamo, J. S. Brooks, *Nat. Commun.* **2013**, 4, 2435.
- [19] G. Gong, C. Zhou, J. Wu, X. Jin, L. Jiang, *ACS Nano* **2015**, 9, 3721.
- [20] S. Zhang, K. Chen, J. Yu, B. Ding, *Polymer* **2015**, 74, 182.
- [21] S. Zhang, H. Liu, N. Tang, J. Ge, J. Yu, B. Ding, *Nat. Commun.* **2019**, 10, 1458.
- [22] S. K. Boda, X. Li, J. Xie, *J. Aerosol Sci.* **2018**, 125, 164.
- [23] L. Persano, C. Dagdeviren, Y. Su, Y. Zhang, S. Girardo, D. Pisignano, Y. Huang, J. A. Rogers, *Nat. Commun.* **2013**, 4, 1633.
- [24] C. Lang, J. Fang, H. Shao, X. Ding, T. Lin, *Nat. Commun.* **2016**, 7, 11108.
- [25] C. Liu, P. C. Hsu, H. W. Lee, M. Ye, G. Zheng, N. Liu, W. Li, Y. Cui, *Nat. Commun.* **2015**, 6, 6205.
- [26] M. Nasir, H. Matsumoto, M. Minagawa, A. Tanioka, T. Danno, H. Horibe, *Polym. J.* **2007**, 39, 670.
- [27] Y. M. Yousry, K. Yao, S. Chen, W. H. Liew, S. Ramakrishna, *Adv. Electron. Mater.* **2018**, 4, 1700562.
- [28] X. Chen, X. Han, Q. D. Shen, *Adv. Electron. Mater.* **2017**, 3, 1600460.
- [29] C. Ribeiro, C. M. Costa, D. M. Correia, J. Nunes-Pereira, J. Oliveira, P. Martins, R. Goncalves, V. F. Cardoso, S. Lanceros-Mendez, *Nat. Protoc.* **2018**, 13, 681.
- [30] H. Li, C. Zhu, J. Xue, Q. Ke, Y. Xia, *Macromol. Rapid Commun.* **2017**, 38, 1600723.
- [31] Z. Li, Z. Xu, Y. Liu, R. Wang, C. Gao, *Nat. Commun.* **2016**, 7, 13684.
- [32] P. Tseng, B. Napier, S. Zhao, A. N. Mitropoulos, M. B. Applegate, B. Marelli, D. L. Kaplan, F. G. Omenetto, *Nat. Nanotechnol.* **2017**, 12, 474.
- [33] A. Zamani, B. Maini, *J. Pet. Sci. Eng.* **2009**, 69, 71.
- [34] S. Taner, B. Pekey, H. Pekey, *Sci. Total Environ.* **2013**, 454–455, 79.
- [35] J. S. Apte, J. D. Marshall, A. J. Cohen, M. Brauer, *Environ. Sci. Technol.* **2015**, 49, 8057.
- [36] K. W. Lee, B. Y. H. Liu, *Aerosol Sci. Technol.* **1982**, 1, 147.
- [37] R. Zhang, C. Liu, P.-C. Hsu, C. Zhang, N. Liu, J. Zhang, H. R. Lee, Y. Lu, Y. Qiu, S. Chu, Y. Cui, *Nano Lett.* **2016**, 16, 3642.
- [38] M. Chinazzi, J. T. Davis, M. Ajelli, C. Gioannini, M. Litvinova, S. Merler, A. P. y Piontti, K. Mu, L. Rossi, K. Sun, *Science* **2020**, 368, 395.
- [39] C. Huang, Y. Wang, X. Li, L. Ren, J. Zhao, Y. Hu, L. Zhang, G. Fan, J. Xu, X. Gu, *Lancet* **2020**, 395, 497.
- [40] J. Nie, X. Chen, Z. L. Wang, *Adv. Funct. Mater.* **2019**, 29, 1806351.
- [41] Y. Feng, L. Ling, J. Nie, K. Han, X. Chen, Z. Bian, H. Li, Z. L. Wang, *ACS Nano* **2017**, 11, 12411.
- [42] P. Li, J. Li, X. Feng, J. Li, Y. Hao, J. Zhang, H. Wang, A. Yin, J. Zhou, X. Ma, B. Wang, *Nat. Commun.* **2019**, 10, 2177.